# Electro-Optical System for Evaluation of Dynamic Inductive Wireless Power Transfer to Electric Vehicles

Luiz A. Lisboa Cardoso[1,2(✉)], Dehann Fourie[2], John J. Leonard[2], Andrés A. Nogueiras Meléndez[3], and João L. Afonso[1]

[1] Centro Algoritmi, University of Minho, Guimarães, Portugal
lisboa.cardoso@ieee.org, jla@dei.uminho.pt
[2] Marine Robotics Group, Massachusetts Institute of Technology, Cambridge, MA, USA
[3] Department of Electronics Technology, University of Vigo, Vigo, Spain

**Abstract.** Inductive lanes that can wirelessly transfer power to moving electric vehicles is a research theme of worldwide interest. The goal is to provide on-the-road recharging, thus extending vehicle's autonomy and reducing battery capacity requirements. These lanes share, however, a common limitation: the power transfer is affected by the lateral displacement of the vehicle, with respect to the center of the lane. In the case of two-wheeled vehicles, such as electric scooters and bicycles, lateral inclination can also be pronounced enough as to interfere with power coupling. In order to experimentally evaluate the characteristics of such vehicular dynamic power transfer schemes, it is then necessary to synchronously log the vehicle's electric data, lateral displacement and attitude. In this paper, the design and implementation of an electro-optical measuring system with these capabilities, based on Light Detection and Ranging (LIDAR) technology and inertial sensors, is reported. A testing range with specific reference geometry, consisting of a corridor of parallel walls, is used to simplify the continuous and accurate estimation of lateral displacement. The design was validated by statistical characterization of the measurement errors, using simulated trajectories. A prototype was built and mounted on a non-electric bicycle, with the first tests confirming its positioning measurement qualities.

**Keywords:** Dynamic wireless power transfer · Inductive lanes · Vehicular power harvesting · LIDAR-based positioning

## 1 Introduction

Successful prototypes of dynamic inductive wireless power transfer (DIWPT) systems have been implemented [1, 2], but no dominant technical solution has been yet established. The prospective benefits of DIWPT, however, largely justify further research efforts to improve this technology. Firstly, the battery capacity requirements of electric vehicles (EV) will be reduced, thus reducing vehicle's initial and life-cycle costs. At the same time, their autonomy will be augmented, depending solely on the


J. L. Afonso et al. (Eds.): GreeNets 2018, LNICST 269, pp. 154–174, 2019.
https://doi.org/10.1007/978-3-030-12950-7_13

widespread use of inductive lanes (i-lanes) in the urban design. The use of multiple EV and i-lanes will, on the other hand, allow more flexible spatiotemporal options for the equilibrium of demand from the power grid, especially if smart vehicle-to-grid (V2G) technology is also considered [3]. All these factors combined shall favor the large-scale adoption of EV, in substitution of thermal-engine powered vehicles.

The great expectation around the future proliferation of dynamic inductive wireless power transfer as a standard technic for providing on-the-road charging [4–6] constitutes the motivation for developing a robust, accurate and inexpensive method for characterizing and evaluating the performance of such systems.

### 1.1 Dynamic Inductive Wireless Power Transfer Systems

In a DIWPT system, when the vehicle moves forward along its path, its pick-up (secondary) coil will cross the magnetic field generated by stationary primary coils placed underneath the floor, along the vehicle's path. The system effectiveness will depend on the appropriated time-spatial coil activation pattern, which is ensured by the power electronic design, but also and fundamentally by good magnetic coupling between the lane and the vehicle, which is ultimately influenced by distance and misalignment between primary and secondary coils.

Even with the use of precise autonomous navigation, some tolerance in the vehicle-to-lane lateral misalignment must be handled by the system [7], this parameter being perhaps the most critical one for human-driven EVs. The measurement of power availability on board of vehicle as a function of lateral displacement over the i-lane is then crucial for the evaluation of a DIWPT system.

### 1.2 Positioning Measurement Techniques

The evaluation of DIWPT requires tracking the position and attitude of an EV relative to the lane, while power is also being monitored. Desirable dynamic accuracies are in the order of one to two centimeters for positioning, and of a few degrees of arc for the estimation of attitude, this latter being achieved by inexpensive inertial measurement units (IMU). All position variables are expected to be sampled tens of times per second, to adequately represent EV trajectories.

In the FABRIC project [8], a recent representative effort in the quest for practical DIWPT, a 100 m long i-lane was tested for vehicle lateral misalignment using RTK Real-Time Kinematic (RTK) Global Positioning System (GPS). In this phase-sensing based variant of Differential GPS (DGPS), positioning accuracies in the order of one centimeter can be achieved [9]. However, current best commercial RTK-GPS receivers have a maximum positioning update rate in the order of 20 Hz [10, 11], which is just marginally acceptable for DIWPT analysis. These systems are also costly and relatively complex, requiring the transmission of a correction signal from a base station to the mobile station whose positioning is being measured.

Optical positioning measurements, using calibrated cameras and visual fiducial markers [12] and, often, infrared dot-markers, can deliver better accuracies at the required speed rates, in indoors tracking applications [13]. However, their simplicity is

diminished when positioning of objects over longer paths, due to the need of increasing the number of coordinated cameras to cover extended areas.

In this work, a special reference geometry was imposed to the test site, allowing the use of LIDARs fixed on an instrument, which is attached to the EV, to directly measure its position. The calculus of the vehicle-to-lane lateral misalignment was significantly simplified by a robust computation neither involving computer vision processing techniques nor requiring inertial data, which are still required for determining vehicle's attitude and forward progress on lane.

## 2 System Design

### 2.1 Requirements

The current system implementation is to be used in the evaluation of DIWPT to lightweight electric vehicles, such as electrically assisted bicycles [14]. For this application, the nominal kinematic parameter limits are given in Table 1.

**Table 1.** Limit parameters assumed for the EV (electrically-assisted bike).

| Parameter | Maximum absolute value |
|---|---|
| Speed | 36 km/h (10 m/s) |
| Lateral acceleration | 3g (3 × 9.81 m/s$^2$) |
| Relative (to lane) yaw angle | 30° |
| Roll angle | 15° |

The range of measurements and the respective desirable order of error magnitude will vary with application and the objectives of the analysis, as well as the specific characteristics of the power train of the vehicle in test. For instance, typical nominal powertrain voltages for electrically assisted bikes are multiple of 12 V, often 24 V or 36 V. Without much information found on general DIWPT evaluation tools currently available, as well as on DIWPT systems specifically implemented for e-bikes [15], values from own experience guided the adoption of the representative values shown in Table 2:

**Table 2.** Target range and precision for vehicle onboard measurements.

| Parameter | Range | Std dev of error |
|---|---|---|
| Lateral displacement | −0.5 to 0.5°m | <2.5 cm |
| DC harvested voltage | 0 to 100 V | 2% of full scale |
| Power train voltage | 0–40 V | 2% of full scale |
| Powertrain demand | 0 to 500 W | 3% of full scale |
| Relative yaw | −30° to 30° | 5° |
| Pitch | −10° to 10° | 2° |
| Roll | −15° to 15° | 2° |

## 2.2 System Overview

The system is implemented as a remote sensing unit to be mounted onto an electric vehicle. Figure 1 shows its high-level block diagram representation: Positional and electric data from the vehicle's WPT receiver (WPT RX) and power-train are collected and wirelessly transmitted via a UHF channel, in real time, to a receiver unit that is connected to a computer (running the Analysis System) through a USB communication port. Electric data coming from the i-lane WPT transmitters (WPT TX) can optionally be monitored and synchronized to the vehicular data.

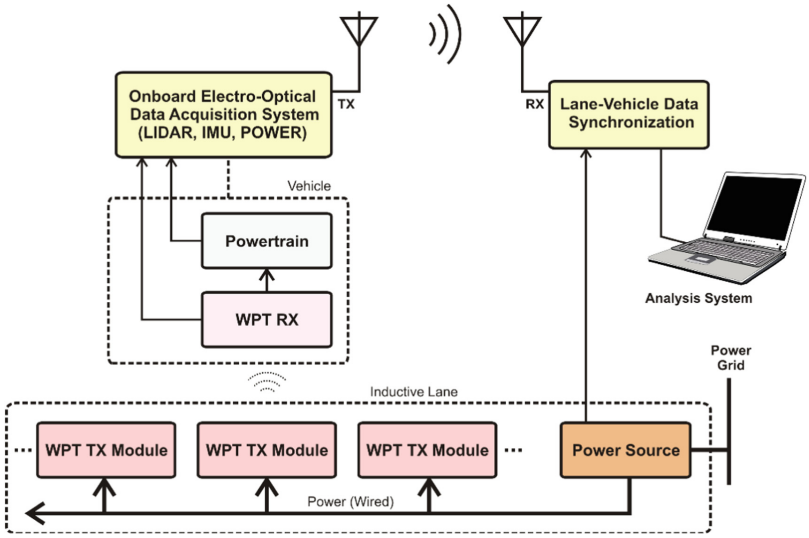


**Fig. 1.** System global architecture, showing vehicle and lane subsystems. All data collected are synchronized and logged for off-line analysis.

## 2.3 Reference Geometry

The system works on the principle that the vehicle's position can be established by knowing the position of a fixed reference geometry. Three individual LIDAR sensors are simultaneously used to measure the lateral distance to the walls of a reference corridor, where the primary inductive modules of the i-lane to be tested lie underneath the floor. Figure 2 illustrates the top view of such configuration, where a single inductive module is under test. Inductive lane modules are aligned and centralized in between the parallel to the walls (A) of a reference corridor. The measurement unit is installed on the electric vehicle running over the inductive lane, indicated in Fig. 2 by a blue dashed curve (C). For lanes of short length, a rear flat surface (B) can be optionally used for referencing the rear LIDAR, if measurements of vehicle speed and longitudinal progress on lane are also required in the analysis.

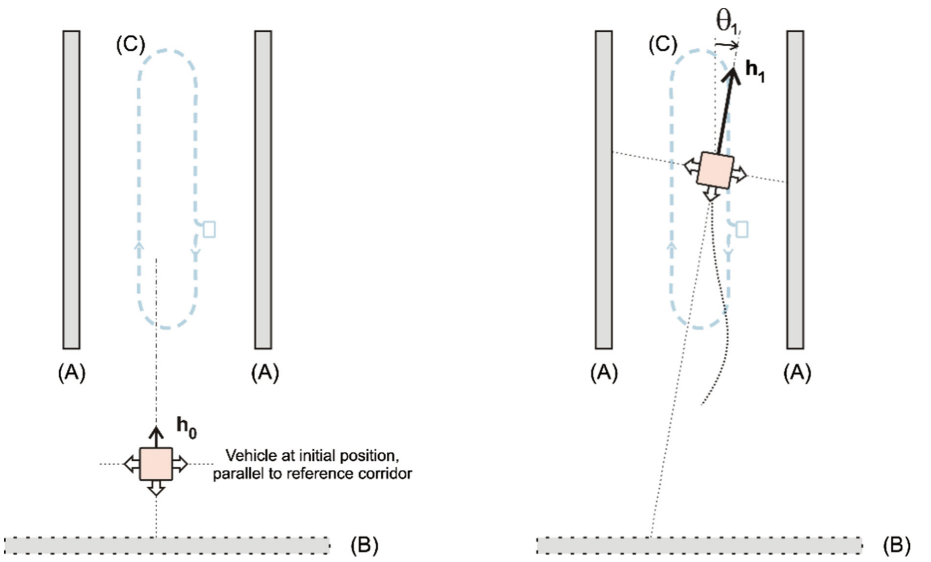


**Fig. 2.** Top view of test range: vehicle at initial position (left) and running in corridor (right). (Color figure online)

### 2.4 LIDAR-IMU Head Design

The heart of the measuring system is the LIDAR-IMU mounting head, drawn in Fig. 3, is a precision machined prismatic rectangular aluminum block of squared base, fixed to the vehicle's structure, mechanically solidary to the pick-up coil used to receive power from the i-lane, where all LIDARs and the IMU are mounted to.

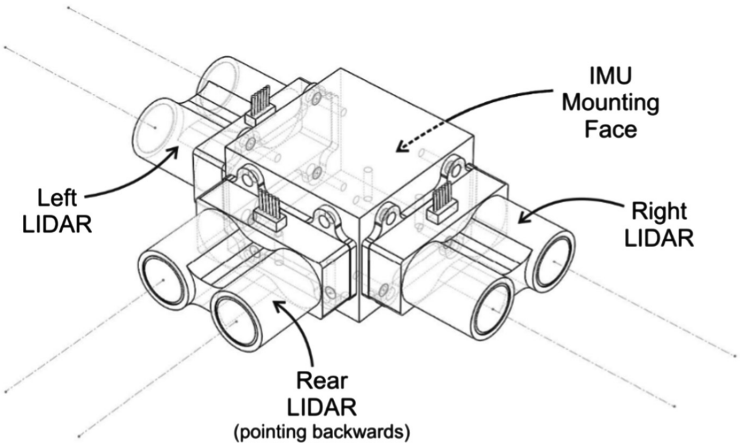


**Fig. 3.** Perspective view of the LIDAR head mounting. An inertial sensor, not shown in the figure, is fixed to the face of the block which is opposite to the face the rear LIDAR is mounted on, with its inertial refence axes orthogonal to the faces of the block.

The left and right LIDAR are align-mounted on opposite parallel faces of the block, with beams pointing opposite directions. A third rear LIDAR is mounted on a face of the block that is orthogonal to the faces of the left and right LIDAR, with its beam pointing backwards, in such a way that all the LIDAR beams are in the same plan, adjusted to be as horizontal as possible, when the assembly is fixed to the vehicle's frame, while the vehicle is resting in a neutral position.

### 2.5 Positional and Attitude Estimation

**Attitude.** The IMU embedded in the instrument continuously computes estimates for the spatial orientation of the vehicle, given by Euler angles, yaw, pitch and roll $(h_k, \rho_k, \gamma_k)$. By construction, yaw (horizontal orientation) and heading (direction of movement) will always coincide, unless the vehicle is skidding on the lane, so these terms are indistinctly used in this work. The last two of these angles, represent inclination with respect to the horizontal and vertical. The absolute yaw $h_k$ estimated by the IMU at any given measurement cycle $k$, however, has to be transformed in the relative orientation angle $\theta_k$, by subtracting the yaw reading obtained at the initially aligned start position ($h_0$, on the left side of Fig. 2) from the current yaw reading (for instance, $h_1$, as shown on the right side of Fig. 2):

$$\theta_k = h_k - h_0 \tag{1}$$

**Progress on Lane.** It is the distance $y$ from the vehicle (LIDAR-IMU head) to the back-wall, taken along the lane. It is measured by computing the projection of the back-LIDAR beam length $d_B(k)$ onto the lane longitudinal axis:

$$y = d_B(k).\cos\ \theta_k.\cos\ \gamma_k \tag{2}$$

If the reference point on the vehicle is not the center of the LIDAR-IMU head, the corresponding coordinate transform should be additionally applied.

**Lateral Displacement.** Whereas the Euler angles are necessary to estimate the distance progressed on the lane, to correct the readings of back LIDAR beams to the back wall, (B) in Fig. 2, the lateral displacement can be directly computed as function of the lateral LIDAR measurements only: Due to deliberate construction of the LIDAR head (Sect. 2.4) and control circuit, beams of the left and right LIDAR at cycle $k$ are both simultaneous and colinear, so the lateral displacement $x_k$ of the EV with respect to center line of the lane can be determined by the proportion of the left and right LIDAR readings, according to (3):

$$x_k = \frac{w_c}{2}\frac{(d_L(k) - d_R(k))}{(d_L(k) + d_R(k) + w_L)} \tag{3}$$

where $d_L(k)$ and $d_R(k)$ are respectively the calibrated readings of the left and right LIDAR (as in Fig. 12), $w_c > 0$ is the width of the corridor and $w_L > 0$ is the distance between opposite external faces of the housing of the measurement unit, from where LIDAR distances are calibrated.

### 2.6 Modeling of Errors

Using (3) to compute the raw lateral displacement, $x_k$, which is a sample of the associated aleatory variable $X_k$, has one more benefit other than not depending on the inertial sensor data processed at the IMU: the standard deviation for $X_k$ can be smaller than those of individual measurements coming from any of the LIDARs, left or right.

Let's assume that both lateral LIDARs have the same behavior and are statistically independent. So, $d_L(k)$ and $d_R(k)$ are samples of aleatory variables $D_L(k)$ and $D_R(k)$, such that:

$$D_i(k) = T_i(k) + E_i, \qquad E_i \sim N\left(0,\, \sigma_L^2\right),\ i \in \{L, R\} \tag{4}$$

where $T_L(k)$ and $T_R(k)$ are the true, but unknown, beam lengths from each LIDAR to its respective target wall, and $E_L$ and $E_R$ are aleatory errors that can be modeled by independent identical normal distributions with zero mean and standard deviation $\sigma_L$. Under these simplifying assumptions, a vehicle running parallel to the corridor will have a normalized standard deviation $\sigma/\sigma_L$ varying according to its relative lateral displacement, as shown in the plot of Fig. 4 (obtained by numerical simulation).

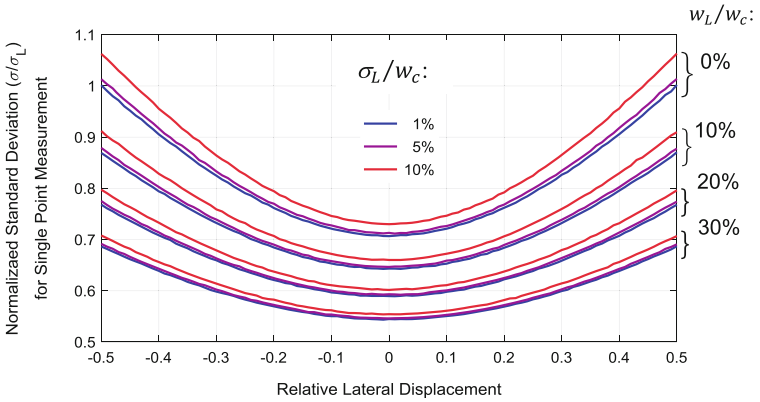


**Fig. 4.** Normalized standard deviation of lateral displacement estimation, given by (2), as a function of the true relative lateral displacement in the corridor (−0.5 means vehicle at left wall and +0.5, at right wall). The curves are shown for different constructive $w_L/w_c$ ratios and relative standard deviations $\sigma_L/w_c$ of the LIDAR measuring errors.

At the limit condition $w_L/w_c = 0$, for small $\sigma_L/w_c$ ratios (5% or less), the standard deviation of $X_k$ can still be up to approximately 30% smaller than $\sigma_L$, when the vehicle is close to the center of the lane, thus improving the quality of the lateral displacement measurement with respect to a single LIDAR measurement, as expected under the assumption of statistical independence of the errors on the two measurements $d_L(k)$ and $d_R(k)$. For the LIDAR components used in the design, the standard deviation errors $E_i$ of are proportional to the distances to be read, $T_i(k)$, ranging around 1% for distances 1 m and above. So, by using calibrated LIDARs, the standard deviation of a single

measurement of the lateral displacement can be reduced up to approximately 0.7%, when the vehicle lies in the central region of the corridor. That corresponds to a ±7 mm error for 2 m wide corridor, when travelling parallel to the reference walls. By filtering or smoothing a series of consecutive measurements along a trajectory, the random error can be further minimized, depending on vehicle kinematics.

In the analysis of DIWPT applications, rather than logging the position of the mounting head itself, often the center of the pick-up coil installed on the EV will be the point of reference for measuring misalignment. Since the pick-up coil is also mechanically solidary to the frame of the vehicle, a simple transform can compute the movement of the coil center (or any other point fixed on the vehicle), based on the estimated position of the center of the LIDAR-IMU block.

## 2.7 Reduction of Error Variance

Assuming a smooth and flat lane with no obstacles, and no intrinsic vehicle vibration due to the power train or other factors, the perturbation on the vehicle movement can be entirely attributed to the human control when riding (or steering), which is ultimately related with human skeletal muscles movements. Since the fastest human hand or finger movements that can be produced lie in the range between 6 to 12 Hz [16], $f_{pos}$, the sampling rate for measuring the vehicle position, can be conservatively set at 60 Hz. A low-pass filter matching this expected bandwidth, with cutting frequency of 12 Hz, is used to condition the sequence of calibrated readings of each LIDAR, reducing the standard deviation of distance estimations.

A Finite Impulse Response (FIR) smoothing window, associated with a low-pass filter with a cutting frequency of 12 Hz and maximally flat response over the pass band, was designed and integrated in the analysis software. Filter coefficients and frequency magnitude response characteristics are shown in Fig. 5.

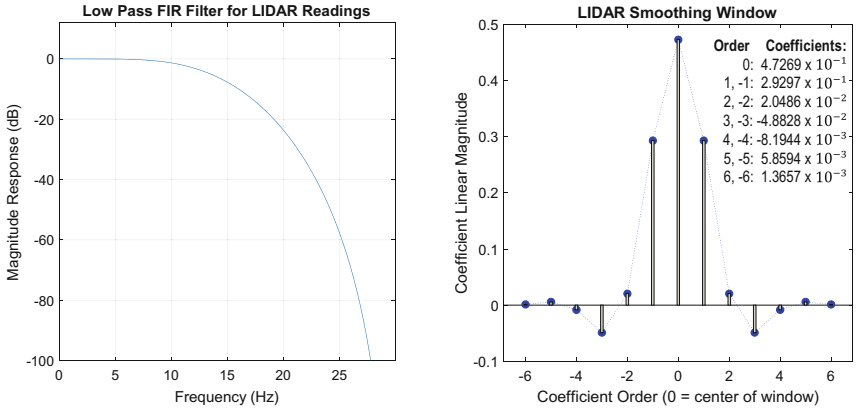


**Fig. 5.** Characteristics of the smoothing window for the LIDAR readings, implemented as a low-pass FIR filter of order 12, for the design LIDAR sampling frequency of 60 Hz.

Assuming an error modeling as in Sect. 2.6, for all LIDARs in the system, the statistical behavior of the error in lateral displacement (3) estimation for any known vehicle trajectory can then be computed by Monte Carlo simulations. Results in Fig. 6 were obtained for the case of a vehicle at the limit design maximum speed of 10 m/s (36 km/h), maneuvering in a sinusoidal pattern along the lane with maximum lateral acceleration of $29.4\,\mathrm{m/s^2}$ (3g, three times the acceleration of the gravity on Earth's surface), within the walls of corridor with width $w_c = 178\,\mathrm{cm}$.

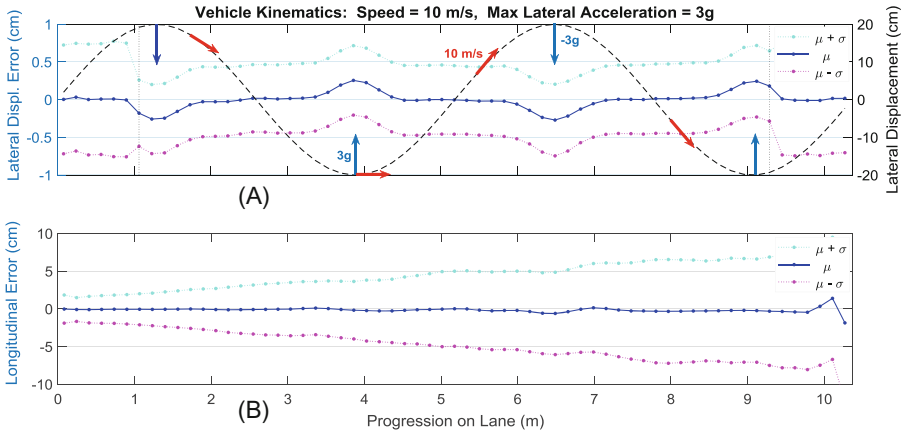


**Fig. 6.** Simulated statistics of positioning error, showing expected mean and standard deviation error for a vehicle on sinusoidal trajectory at limit design kinematics. (A) Upper graph shows error behavior in vehicle's lateral displacement measurement, as the vehicle progresses forward on the lane; (B) lower graph shows tendency for errors in longitudinal position.

The error pattern in lateral displacement is regular along the vehicle's trajectory, with mean μ zero most of the time, except at maximum excursions, when the measurement will lag the movement, resulting in a biased error up to approximately 3 mm. The standard deviation of the error remains practically constant, about 5 mm along all the lane, except for the first and last $N/2$ measurements on the lane, due to the smoothing window filter order N, where it raises to values of the standard deviation of a single measurement. These values will vary proportionally to the intrinsic standard deviation characteristic of the LIDAR readings, which will depend on the actual LIDAR model and the geometry $(w_c)$ of the reference corridor being used.

## 2.8 Longitudinal Error

In Fig. 6(B), the longitudinal error can be noted to be unbiased along all the vehicle's path. The standard deviation, however, starts with a minimum value $\sigma_L$ in the order of 2 cm, and increases approximately in proportion to the progression on the lane, due to the dependency of the forward displacement estimation on a single back LIDAR reading, which has a standard deviation that is also proportional to the distance to the back wall, set 2 m behind the corridor entrance, the point of zero progression.

This behavior limits the application of the proposed configuration to lane modules up to about 6 m long, in the case secondary measurements related to forward movement of a vehicle are to be performed. For lateral displacement measurements, there is no such limitation, if the reference corridor is long enough to enclose the lane module to be evaluated.

## 2.9 System Block Diagram

**Onboard Wireless Electro-Optical Monitor.** This unit, as detailed in the block diagram of Fig. 7, has three LIDARs, one pointing right, one pointing left and one pointing backwards. All these LIDAR (Garmin Lite v3) and the IMU (Bosch BNO-055) are connected by a 400 kbit/s I2C bus to a master 32-bit STM32F103 microcontroller, the "Position Processor", which runs a supervisor program that every 16.67 ms gets the distance measurements from the LIDAR sensors, the Euler angles from the IMU, and the vehicle electric data coming through a dedicated 230.4 kbaud/s asynchronous serial bus from another 32-bit microcontroller, named the "Electric Data Processor". To accommodate different timing requirements, data from different sensors are buffered in one cycle and transmitted in the next cycle.

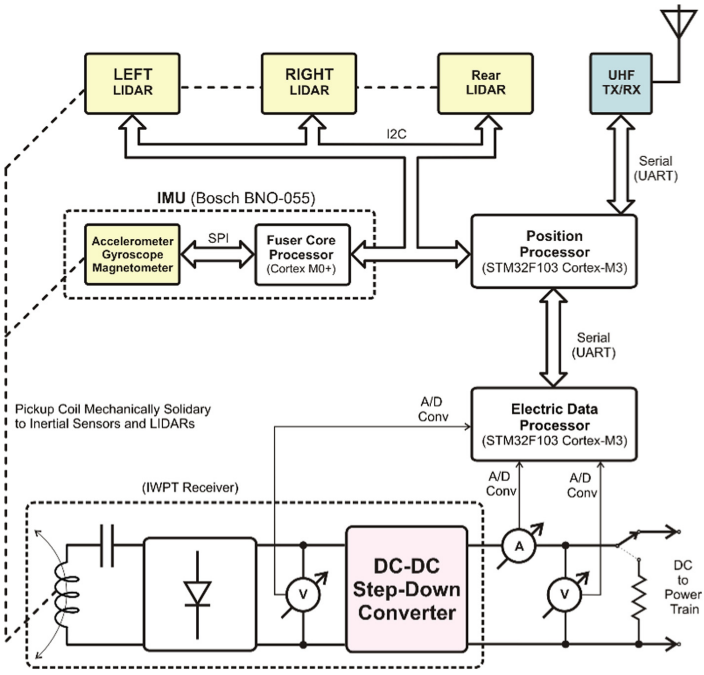


**Fig. 7.** Electro-optical data acquisition system architecture on board of the electric vehicle.

The adoption of a sampling period $T_{pos} = 16.67$ ms for the positional data, corresponds to a sampling frequency, $f_{pos}$, of 60 Hz, which implies (Nyquist Theorem) in a maximum tolerable bandwidth for the vehicle movement $B_{pos} = f_{pos}/2 = 30$ Hz.

Based on the predicted bandwidth limitation of 6 to 12 Hz, as seen in Sect. 2.7, all LIDAR calibrated measures can be further subjected to a low pass filter to reduce the variance of measurement errors.

The Electric Data Processor, on the other hand, performs analog-to-digital conversion on the signals coming from two voltmeter channels, which share a common ground reference, and a third channel sending data from a galvanically isolated Hall-effect amperemeter. When monitoring the electric vehicle, the amperemeter channel is intended to be associated with one of the voltage channels in a series-parallel connection. Power is computed by discrete integration of the product of these readings. The sample rate of the electric signals, $f_{power}$, was set to 6 kHz, a hundred times greater than $f_{pos}$. A new power estimate, integrated over the most recent 16.67 ms interval, is produced every $T_{power} = 166.7\,\mu s = 16.67\,ms/100$, and becomes available to be asynchronously read upon request of the Position Processor. The rms values for all other electric signals are similarly computed. In this manner, although the electric data is read just once every 16.67 ms, there will be no loss of information on the total power and average effective values of voltages and current, except where induced by noise or arithmetic rounding errors, if the maximum electric data bandwidth is limited to $B_{power} = f_{power}/2 = 3$ kHz.

The power transferred in a DIWPT configuration is expected to depend mostly on: (i) the relative position of the WPT receiver (in the vehicle) and the WPT transmitter (in the lane), which is also assumed to be bandwidth limited to $B_{pos}$; (ii) the fluctuations on the power demand of the powertrain; and (iii) the switching state (ON/OFF) and time response of the power electronics driving the WPT transmitter and receiver. To facilitate evaluating the profile of the maximum WPT as a function of lateral displacement, the WPT transmitter should be kept always activated, and the load coupled to the WPT receiver, on board of the vehicle, should be made constant. The system developed is then furnished with a dummy DC load to momentarily replace the power train during maximum transferred power profile tests.

Positional and electric data are packed together into 26-byte frames, including a time tag and a check-sum word, and periodically transmitted over UHF at 38400 baud/s. The UHF radio-modem used can be programmed to output power levels up to 20 dBm (100 mW), using any of 100 channels in the 433.4–473.0 MHz band. This is enough power to achieve virtually errorless transmission up to 30 m range in free space, a distance by design much larger than the length of the inductive modules and lane segments the equipment was built to monitor.

**Remote Vehicle Data Logger.** This unit receives and logs the vehicle data to a "Data Log Computer", as shown in the block diagram of Fig. 8. It can also optionally monitor and log electric data coming from the i-lane. A "Lane Activity Log Processor" acquires electrical data from the lane and merges it into data frames coming from the electro-optical measuring system installed on board of the vehicle. Because of the delays involved in measuring and transmitting over the UHF link the positional and electrical data coming from the EV, the "Lane Activity Log Processor" has to introduce compensatory delays in the lane data stream, to time-align both data sources.

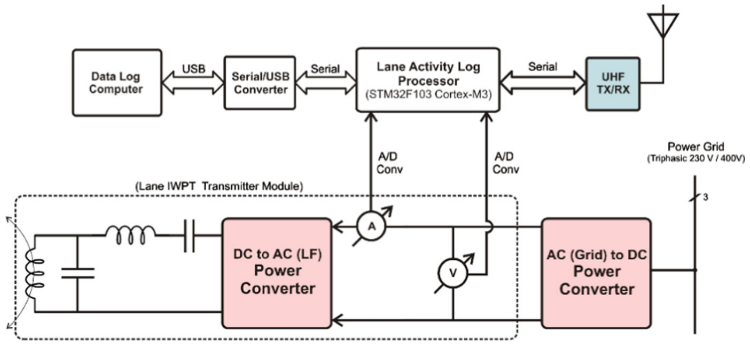


**Fig. 8.** System architecture on the lane side: real time data coming from vehicle is received and associated with simultaneous electric data sampled from the lane WPT transmitter module.

### 2.10 Supplementary System Sensors

Beyond the LIDAR-IMU based power and positioning monitoring system, other two independent subsystems were integrated into the developed equipment as general tools for future use, in support of the evaluation of DIWPT of EVs:

**Scanning LIDAR.** A short range (8 m) scanning LIDAR that rotates continuously at 5 to 15 Hz (300 to 900 rpm), providing 360º horizontal scan, with up to 4000 distance readings per second (model A2M8, manufactured by Shanghai Slamtec Co., Ltd.) It will allow future investigation of simultaneous localization and mapping (SLAM) techniques [17] as an alternative for positioning determination. Its current function is solely to provide panoramic LIDAR scene visualization, for checking consistence of the positioning data logged in the test runs.

**Voltage Data Logger.** A four-channel, differential analog-to-digital converter, of up to 40 kSamples/s per channel, data-logging system, for monitoring other electrical signal on board of the vehicle was also installed in the rack. The gain of each channel can be independently programmed to allow measuring signals up to $\pm 100$ V in amplitude. Data can be logged locally on disk, for posterior analysis, or relayed over a Wi-Fi link, for remote real-time system monitoring. It can, for instance, be used as a redundant power logging system, if additional current sensors are installed on the EV.

## 3 Implementation

### 3.1 Power Measurement Module

The implementation of power measurement subsystem was conceived and cost-optimized to evaluate electrically assisted DIWPT bicycles [14, 15]. It has two independent voltmeters and one amperemeter. One of the two voltmeter channels is associated with the amperemeter channel to provide power readings of the input to the

power train or the substitute dummy load. The other voltmeter channel can be used, for instance, to measure the voltage at the DC output of the WPT receiver and pattern the voltage and power availability at any given position. All channels and the power product are sampled at 6 kHz and integrated over the most recent period of 16.67 ms, to provide readings of rms values over the positioning measurement cycles. The Hall sensor used in the design (ACS-712-30A, from Allegro MicroSystems, LLC) converts current to voltage with a factor of 66 mV/A, and a worst-case output accuracy of 1.5% at 25 °C, due to non-linearity. The zero current level corresponds to a 2.5 V output of the Hall sensor. The voltmeter channels have a maximum 0.5% error due to restive networks (voltage divisor). All conditioned signals are presented before the A/D (analog to digital) converter inputs of the microcontroller (STM32F103, from ST Microelectronics), with a reading range from 0 to 3.3 V at 12-bit, with a maximum total conversion error of ± 7.5 LSB (least significant bit) and a typical maximum error of ±4.3 LSB at 25 °C, as shown in Table 3.

**Table 3.** Electric data typical maximum errors at 25 °C for uncalibrated single measurements.

| Channel | Reading | Range | Multiplier | Uncalibrated error |
|---|---|---|---|---|
| $V_H$ | High side voltage | 0 to 134.2 V | 1/41.6667 | 0.5% + 4.3/4096 = 1.6% |
| $V_L$ | Low side voltage | 0 to 45.1 V | 1/13.6667 | 0.5% + 4.3/4096 = 1.6% |
| $I$ | Current | −12.1 to 30 A | 66 mV/A | 1.5% + 4.3/2703 = 3.1% |
| $P_H$ | High side power | −1.6 to 4 kW | (indirect) | 1.6% + 3.1% = 4.7% |
| $P_L$ | Low side power | −545 to 1353 W | (indirect) | 1.6% + 3.1% = 4.7% |

The instantaneous maximum power error (of a single measurement), given by the product of I × $V_k$, can be computed by adding the relative errors of I and $V_k$, that is, 1.6% + 3.1% = 4.7%. System calibration, however, can greatly compensate errors due to non-linearity, leaving practically only the typical random A/D conversion errors of respectively 1.1% and 1.6% for voltages and current. This gives a precision of 2.7% for instantaneous power readings, a figure that, for slow varying signals, can be further reduced when integrating the $N = 6\,\text{kHz}/60\,\text{Hz} = 100$ power samples in the average power calculation performed on the Electric Data Processor.

### 3.2 Attitude, Positioning and Electric Data Synchronization

Each single LIDAR measurement computed and logged at $f_s = 60$ samples per second, is obtained from the integration of individual pulse readings at a faster rate (>10 kHz), until a good correlation peak is detected in the return signal, backscattered by the reference walls. The maximum number of scan pulses used in this scan process can be programmed, and was experimentally optimized at 16, for a good balance between fast, stable and accurate readings. The correlation analysis of each of these pulse trains is accomplished in the mean time $t_{corr} = 2$ ms.

Euler angles are also logged at 60 samples per second, but their readings come from an inner data fusion estimation process running on the IMU, at a rate $f_{IMU} = 100$ Hz. Since $f_s$ and $f_{IMU}$ are asynchronous, the IMU data can be up to $1/f_{IMU} = 10$ ms "old" with respect to the reading time. Similarly, the supervisor program running on the Position Processor executes several tasks along each 16.67 ms cycle, in such a manner that different sensors are not read at the same time. UHF transmission is not an instantaneous process as well: beyond the almost negligible propagation delay, the data is cached into a dedicated modulation processor and transmitted at 38.4 kbaud/s. Careful analysis and experimental timing evaluation of all processes involved in the computation of measurements resulted in the simplified timing diagram in Fig. 9, which shows the main events of the system, from LIDAR reading start until all data from vehicle is available at the stationary receiver on the lane side. A new data set of measurements is available every 16.67 ms.

Precise analysis of the logged data should take these delays into consideration, to time-align the lagging lateral displacement measurement (based only on LIDAR readings), the attitude measurements, the EV electrical measurements and the electric measurements coming from the i-lane.

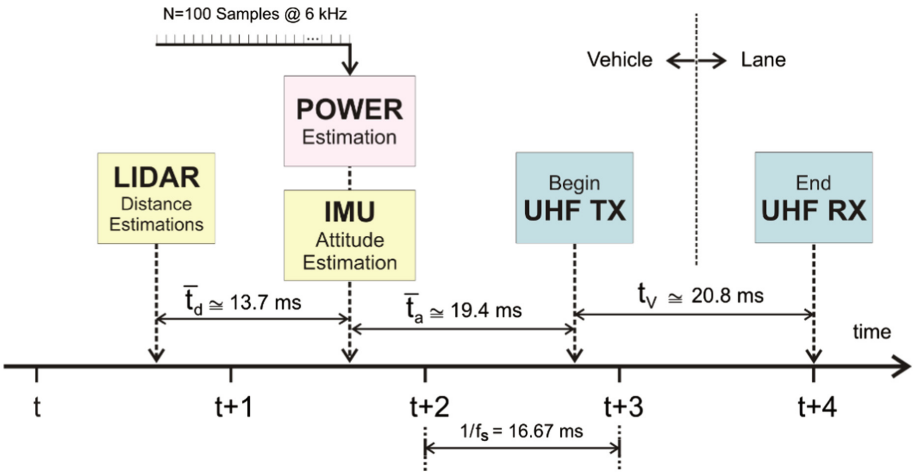


**Fig. 9.** Time line of main events in the system, from measurements on board of EV to UHF transmission and synchronization with lane data.

### 3.3 Prototype Integration

The electronics of the system were organized into two printed circuit board units, one for the LIDAR-IMU control and the other for power measurement, both using STM32F103 32-bit microcontrollers (Cortex-M3 core architecture), with a clock speed of 72 MHz (Fig. 10).

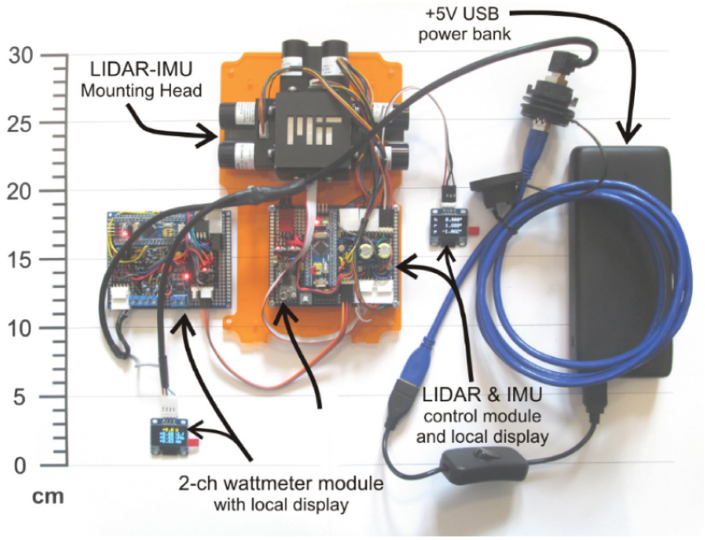


**Fig. 10.** Modules of the electro-optical measurement unit electrically connected during functional tests, before being mechanically integrated (except the power bank) into an IP68 housing.

The LIDAR-IMU control and the power measurement units were stacked and housed in an IP68 (according to IEC standard 60529) polycarbonate enclosure with clear lid, resulting in a total $w_L = 14$ cm (LIDAR box width). The only external electrical wired connections, those for power, voltage and current sensor inputs, uses IP68 compatible connectors. Inside the enclosure and visible through the clear lid were installed two organic LED (OLED) displays, for local reading of measurements made by each of the two modules. The watertightness of the assembly was, however, severely impaired by the holes drilled to let the LIDAR beams and their respective back scattering rays pass through the laterals of the box. For dust protection, 2 mm cast transparent acrylic windows were introduced to cover the LIDAR beam holes. These acrylic windows are also transparent (>85% transmission) at the 905 nm wavelength (infrared) emission of the LIDAR type used. Their effect in attenuating and delaying the LIDAR signals can be compensated by calibration procedures, with the maximum detection range being degraded, but experimentally verified to be still over 10 m, enough for the application. For testing vehicles outdoors in arbitrary weather, it would be necessary to redesign the LIDAR protection windows, so that the adequate watertightness grade is met.

The power demand of the electric powertrain will depend on the acceleration and mechanical drag forces imposed to the vehicle, greatly varying along the vehicle progression on its path. A useful test condition is then to force the power consumption to the nominal maximum power demand of the powertrain. This can be achieved by momentarily replacing the powertrain circuit by a resistive dummy load of appropriated value. Such resistive load was also integrated in the prototype, as seen in Fig. 11(C), to facilitate the evaluation tests.

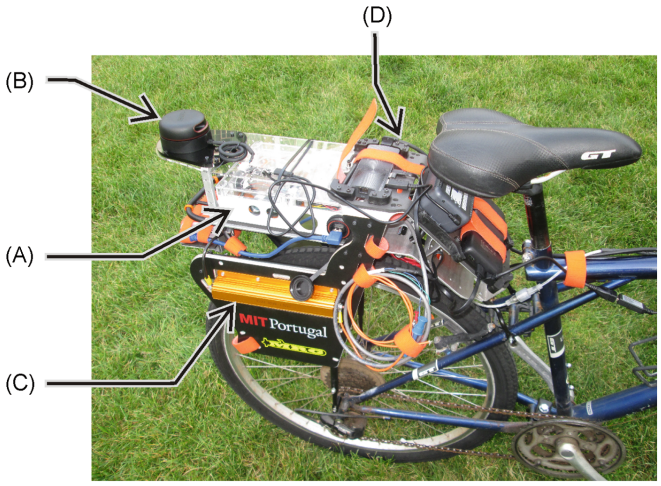


**Fig. 11.** UHF wireless electro-optical measurement unit (A) installed on a non-electric bicycle, for the initial positioning tests. Other system elements on the same assembly: (B) rotating LIDAR; (C) resistive loads and heatsink, mounted on both sides of vehicle; and (D) redundant voltage data logger model DI-1120, from DATAQ Instruments Inc., and management system, running on a Microsoft Windows 10 Pro PC Stick, manufactured by Azulle Tech.

# 4 Experiments and Results

## 4.1 LIDAR Calibration

The lateral LIDARs were calibrated using 9 reference distances from approximately 25 cm to 145 cm, and the back LIDAR using 5 reference distances from 112 cm to 766 cm. According to fabricant (GARMIN) of the LIDARs model Lite v3 used, the non-linearity in the LIDAR readings, as seen in Fig. 12, is expected, when measuring distances of 1 m and shorter (yellow shaded area). An observed increase in the standard deviation of readings at distances less than 0.45 m, however, strongly restricts practical operation of these LIDARs at too short range (gray shaded area).

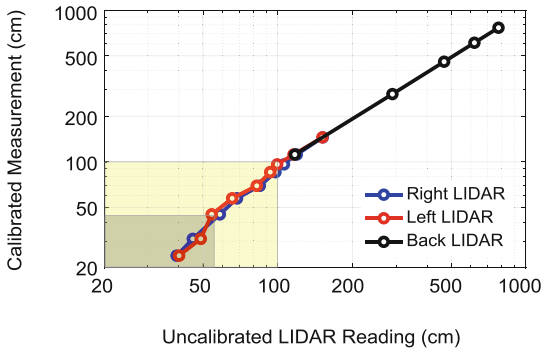


**Fig. 12.** LIDAR calibration curves experimentally obtained. (Color figure online)

### 4.2 Test Site Configuration

The ideal dimensions of the reference corridor depend on: (i) the range of magnitude of the lateral displacements to be measured; (ii) the maximum expected tilt angles of the vehicle, with respect to the corridor longitudinal axis; and (iii) the characteristics of the LIDAR used in the design.

According to the manufacturer (GARMIN) of the LIDARs used (model LIDARLite v3), the maximum range of detection, $d_{max}$, is 40 m, with an error of $\pm 1\%$ in the mean value read, and another $\pm 1\%$ error due to dispersion, for distances above 1 m, with non-linear behavior when reading distances less than 1 m. From experimentation, it was verified that the standard deviation of the distance measurements is reduced (down in the 7 mm to 9 mm range) at the distances of approximately 0.6 m to 1.2 m, increasing rapidly as the distance falls below 0.5 m, and proportionally to distance itself, at distances above 1.2 m.

Non-linearity in the readings can be compensated by calibration procedures, if operation distances are kept above $d_{min} = 0.5\,\text{m}$. The reference corridor width $w_c$ should be such that the minimum distance from the LIDAR head to the wall, at the condition of maximum displacement from the center of lane, should be not less than the above marked minimum recommended operation distance $d_{min}$ for the LIDAR. Thus, a good choice $w_{min}$ for the minimum value of the corridor width, without experimenting LIDAR increased dispersion errors, would be expressed by:

$$w_{min} = d_{min} + d_L + w_L + d_{min} = 2d_{min} + d_L + w_L, \tag{5}$$

where $d_L$ is the maximum anticipated lateral displacement width for the vehicle and $w_L$ is an equipment parameter, as defined in (3).

The maximum detection range $d_{max}$ also restricts the maximum corridor width, $w_{max}$. Considering the vehicle can assume relative heading $(\alpha)$ and pitch $(\beta)$ angles limited in absolute values respectively to $\alpha_{max}$ and $\beta_{max}$, then:

$$w_{max} \leq d_{max}.\cos(\alpha_{max}).\cos(\beta_{max}), \tag{6}$$

There is, however, one more condition on the maximum value of $w_c$, that can be derived by requiring the LIDAR beam not to touch the floor, what would invalidate the simple expression in (3) for calculating the lateral displacement. The limit condition is when the vehicle is maximally tilt (roll angle) inside the corridor:

$$\frac{w_{max}}{cos(\alpha_{max})} \leq \frac{h_{LIDAR}}{sin(\beta_{max})}, \tag{7}$$

where $h_{LIDAR}$ is the height of the center of the LIDAR mounting head above the floor plane. So, reuniting conditions given in (6) and (7), the maximum corridor width, $w_{max}$, can be expressed by:

$$w_{max} = cos(\alpha_{max}).\min\left\{d_{max}.\cos(\beta_{max}), \frac{h_{LIDAR}}{\sin(\beta_{max})}\right\}, \tag{8}$$

For a bicycle, a typical $d_L$ of interest will be around 1 m, so the desirable minimum corridor width to be used with measurement unit, as given by (5), should be 2.15 m. During the experiments with the bicycle, it was verified that heading (relative to lane longitudinal axis) and roll angles, under normal ridging conditions, were respectively limited to 30° and 15°. Using (8) and considering a mounting height of 1 m and the characteristic $d_{max}$ of the LIDAR used in the design, results that the maximum corridor width should be approximately 3.35 m.

In the first test runs herein reported, a corridor 1.778 m wide (Fig. 13) was used, due to its prompt availability (near our lab). This value lies outside the calculated ideal corridor width range. The consequence is that, for this width, lateral displacements estimations $d_L > 1.778 - 2 \times 0.5 - 0.15 = 0.628\,\text{m}$ are expected to have increased

**Fig. 13.** Left: experimental setup temporarily established during night time, in one of the corridors of MIT Computer Science and Artificial Intelligence Laboratory. Right: tracking the bicycle on the video, as a reference for data consistency check.

dispersion errors. In practice, however, there was no problem with that, because, for such a narrow corridor, its is difficult to ride with lateral misalignments much greater than 0.63 m, due to the increased risk of collision with the walls.

### 4.3 Trajectory Reconstitution

As a simplification, without any loss of generalization, we assume that the pick-up coil is parallel to the LIDAR (beam) plan, and its center is located at a fixed distance $H_C$ below the center of the LIDAR-IMU mounting head. The chart on Fig. 14(C), shows a trajectory reconstruction generated by the interactive analysis program written in MATLAB, from MathWorks, using $H_C = 62\,\text{cm}$. The green dots are computed applying (2) and (3) to the IMU (B) and raw LIDAR data. The black curve on (C) is the estimated trajectory using filtered LIDAR data (A) instead. Since the bicycle in which the measurement unit was installed for the initial tests had neither electric power train nor energy harvesting devices, no electric data is associated to the trajectory.

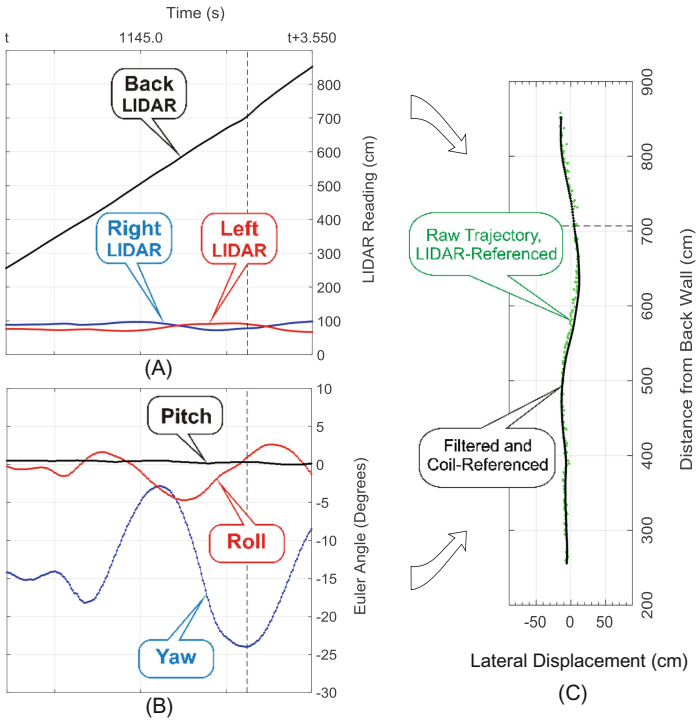


**Fig. 14.** Reconstitution of the trajectory of the center of a pick-up coil fixed on vehicle frame (C), based on LIDAR readings (A) and Euler angles (B). (Color figure online)

The unavailability of an accurate reference instrument also capable of dynamically measuring the trajectories, in the same way the presently developed instrument does, made it difficult to verify experimentally the measurement errors, currently only estimated by simulation. The computed trajectories were still compared to those obtained by video tracking Open Source Physics software [18], as shown in Fig. 13 (right), with consistent qualitative results. In this fist experiments, the low resolution of the camera used, however, limited the accuracy of trajectory estimation by the video tracking software, so far not permitting a useful numeric comparison with trajectories measured by the developed electro-optical equipment.

## 5 Conclusion

An electro-optical measurement instrument for analyzing dynamic wireless power transfer configurations was designed, implemented and tested for positioning. The combined use of LIDARs, IMU and a testing range with controlled geometry resulted in a simple, robust and potentially accurate technique to log the power transfer profile as function of lateral misalignment, critical for assessment of DIWPT schemes.

Statistical simulations indicate the capability of lateral displacement measurements with errors smaller than the base precision of the LIDAR components used, when testing vehicles with speeds up to 36 km/h and lateral accelerations up to three times the acceleration of gravity. Initial experiments with a prototype, specifically built for evaluating electrically assisted bicycles running on short inductive lanes (<10 m), confirm its adequacy of use, and indicate potential to achieve dynamic accuracies better than 1 cm, provided a calibration procedure is previously executed. Testing of the prototype will continue to fully explore its qualities as a DIWPT evaluation tool.

The measurement technique developed can be extended to larger and faster electric vehicles, and longer lane segments. For that, it is required that an appropriated reference corridor is set around the inductive lane under evaluation.

**Acknowledgments.** This research was partially supported by grant SFRH/BD/52349/2013 and project ESGRIDS – Enhancing Smart GRIDs for Sustainability, POCI-01-0145-FEDER-016434, both from FCT, the Portuguese funding agency supporting science, technology and innovation, and the MIT-Portugal Program. The authors are also thankful to R. Wiken, for his support with the mechanical implementation of the prototype at the MIT-CSAIL Machine Shop, to M. Brennan, for her generous donation of the bike used in the tests, and to L. Zvereva, who volunteered as a pilot in the first runs.

## References

1. Mi, C.C., Buja, G., Choi, S.Y., Rim, C.T.: Modern advances in wireless power transfer systems for roadway powered electric vehicles. IEEE Trans. Ind. Electron. **63**, 6533–6545 (2016)
2. Song, K., Koh, K.E., Zhu, C., et al.: A review of dynamic wireless power transfer for in-motion electric vehicles. In: Coca, E. (ed.) Wireless Power Transfer. IntechOpen, Rijeka (2016)
3. Yu, R., Zhong, W., Xie, S., et al.: Balancing power demand through EV mobility in vehicle-to-grid mobile energy networks. IEEE Trans. Ind. Inform. **12**, 79–90 (2016)
4. Covic, G.A., Boys, J.T., Budhia, M., Huang, C.: Electric vehicles – personal transportation for the future. World Electr. Veh. J. **4**, 693–704 (2010)
5. Ahn, S., Cho, D.-H.: Future wireless power transportation system. In: 2013 Asia-Pacific Microwave Conference Proceedings (APMC), pp. 468–469 (2013)
6. Bosshard, R., Kolar, J.W.: Inductive power transfer for electric vehicle charging. IEEE Power Electron. Mag. 22–30 (2016). https://doi.org/10.1109/mpel.2016.2583839
7. Mazharov, N.D., Hristov, S.M., Dichev, D.A., Zhelezarov, I.S.: Some problems of dynamic contactless charging of electric vehicles. Acta Polytech. Hungarica **14**, 7–26 (2017)
8. Laporte, S., Coquery, G., Revilloud, M., Deniau, V.: Experimental performance assessment of a dynamic WPT system for future EV in real driving conditions. In: 3rd Workshop on EV Systems, Data, and Applications (EV-Sys 2018), Proceedings of the 9th ACM International Conference on Future Energy Systems, Karlsruhe, Germany, pp. 570–578 (2018)
9. Feng, Y., Wang, J.: GPS RTK performance characteristics and analysis. J. Glob. Position Syst. **7**, 1–8 (2008)
10. Supej, M., Čuk, I.: Comparison of global navigation satellite system devices on speed tracking in road (Tran)SPORT applications. Sensors **14**, 23490–23508 (2014)
11. Leica Geosystems AG: Leica GS18 T Data sheet, pp. 1–2 (2017)

12. Lightbody, P., Krajník, T., Hanheide, M.: A versatile high-performance visual fiducial marker detection system with scalable identity encoding. In: Proceedings of the Symposium on Applied Computing, pp. 276–282. ACM, Marrakech (2017)
13. Mossel, A.: Robust 3D position estimation in wide and unconstrained indoor environments. Sensors **15**, 31482–31524 (2015). https://doi.org/10.3390/s151229862
14. Association française de normalisation (AFNOR): European Standard NF EN 15194(2009)
15. Cardoso, L.A.L., Martinez, M.C., Melendez, A.A.N., Afonso, J.L.: Dynamic inductive power transfer lane design for e-bikes. In: 2016 IEEE 19th International Conference on Intelligent Transportation Systems (ITSC), pp. 2307–2312 (2016)
16. Freund, H.-J.: Time control of hand movements. Prog. Brain Res. **64**, 287–294 (1986)
17. Thrun, S., Leonard, J., Siciliano, B., Khatib, O.: Simultaneous localization and mapping. In: Siciliano, B., Khatib, O. (eds.) Springer Handbook of Robotics, pp. 871–889. Springer, Heidelberg (2008). https://doi.org/10.1007/978-3-540-30301-5_38
18. Brown, D.: Tracker - Video Analysis and Modeling Tool, version 5.0.6 (2018)